Acoustic wave propagation at nonadiabatic conditions: The continuum limit of a thin acoustic layer

Y. Ben-Ami and A. Manela[*]

Faculty of Aerospace Engineering, Technion–Israel Institute of Technology, Haifa 32000, Israel

Existing works on sound propagation in rarefied gases have focused on wave transmission at adiabatic conditions, where a reference uniform equilibrium state prevails. To extend these studies, we analyze the propagation of acoustic waves in a slightly rarefied gas at nonadiabatic conditions, where arbitrarily large reference temperature and density gradients are imposed. Considering a planar slab configuration, constant wall heating is applied at the confining walls to maintain the nonuniform reference thermodynamic distributions. Acoustic excitation is then enforced via small-amplitude harmonic wall oscillations and normal heat-flux perturbations. Focusing on continuum-limit conditions of small Knudsen numbers and high actuation frequencies (yet small compared with the mean collision frequency), the gas domain affected by wall excitation is confined to a thin layer (termed "acoustic layer") in the vicinity of the excited boundary, and an approximate solution is derived based on asymptotic expansion of the acoustic fields. The application of thermoacoustic wall excitation necessitates the formation of an ever thinner "thermal layer" that governs the transmission of the wall's unsteady heat flux into sound waves. The results of the approximate analysis, supported by continuum-model finite differences and direct simulation Monte Carlo calculations, clarify the impacts of system nonadiabaticity and the gas kinetic model of interaction on sound propagation. Primarily, reference wall heating results in an extension of the acoustic layer and consequent sound-wave radiation over larger distances from the wall source. Considering the entire range of inverse power law (repulsion point center) interactions, it is also found that wave attenuation is affected by the kinetic model of gas collisions, yielding stronger decay rates in gases with softer molecular interactions. The results are used to generalize the counterpart adiabatic-system findings for the amount of boundary heat flux required for the silencing of vibroacoustic sound at nonadiabatic reference conditions.

I. INTRODUCTION

Prevailing analyses of sound wave propagation in fluids commonly consider an adiabatic reference state of the medium, where the acoustic field perturbs the system's initial conditions of uniform temperature and density [1,2]. Yet, in various realistic setups, the propagation of acoustic waves should be affected by nonuniformities in the reference temperature and density fields, leading to variations in the gas acoustic wave speeds and attenuation rates compared with their adiabatic counterparts. Within the context of continuum gas dynamics, several works have been carried out to investigate the passage of acoustic waves through nonisothermal atmospheres (see, e.g., Refs. [3–5], and works cited therein). While incorporating the effect of gravity force on sound propagation, most of these works have not considered the dissipative impacts of gas viscosity and heat conductivity,

---

*Corresponding author: amanela@technion.ac.il

which are small at atmospheric length scales. In a single work, Campos [6] mentioned the presumed influence of viscous dissipation in his problem formulation, yet a solution where this effect was quantified was not derived.

The propagation of sound waves in systems characterized by small length scales (of the order of the molecular mean free path) or short time scales (similar to the kinetic mean free time) inevitably couples compressibility and viscous effects. At such conditions, the continuum description breaks down, and gas rarefaction must be taken into account in the framework of gas kinetic theory. Focusing on such setups, acoustic wave generation has been studied in a considerable number of works, investigating vibroacoustic (see Refs. [7–11] and papers cited therein) and thermoacoustic [12–17] sound transmission in rarefied gases, driven by mechanical and thermal boundary excitations, respectively. While covering the entire spectrum of gas rarefaction regimes, these works have commonly assumed wave propagation through *adiabatic* gas layers, where a reference uniform equilibrium state prevails. A study on the counterpart effect of *reference state nonuniformities* is therefore lacking, and provides the topic for the present work. Focusing on near-continuum conditions, this constitutes a significant extension over existing analyses, since the reference-state nonhomogeneities, coupled in the governing acoustic equations, considerably affect the mathematical formulation and consequent characteristics of sound propagation, as described herein.

Apart from the fundamental interest in investigating the above problem, the consideration of the effects of reference temperature and density variations on sound transmission appear relevant in a sequence of applications. Within the context of noncontinuum flows, nonuniform reference states are encountered in high-frequency microscale cooling devices [18,19], RF-MEMS attenuators [20,21], and optoacoustic transducers, where both mechanical and thermal film vibrations are excited through laser pulsations [22,23]. Other setups include thermoacoustic engines and refrigerators [24,25], induction motors [26], synthetic jet cooling machines [27,28], and thermophone devices [29–31]. Specifically for the thermophone apparatus, existing theoretical studies have been carried out under the assumption that the gas is initially set at a uniform equilibrium state (see, e.g., Refs. [32–34], and cited works). Such conditions are nevertheless difficult to realize in practice due to the difficulty in withdrawing heat from the system during the cooling half-cycle. In effect, the boundary heat flux oscillates around a certain nonzero mean value, resulting in a steady temperature gradient of the gas. It is therefore of practical interest to reassess the thermoacoustic gas response in the presence of thermally nonuniform steady conditions, which are expected to affect the amount of boundary heat flux required for achieving vibroacoustic sound cancellation [17]. While the general approach of achieving vibroacoustic sound reduction through unsteady heating has been recently tested in an experiment [31], it could not verify the ratio of heat flux to mechanical work needed to perform noise silencing. Reassessing this ratio, in addition to performing a general investigation on the effect of system nonadiabaticity on sound transmission in a gas, constitute the main goals of the present work.

Adopting a simple model setup, we consider a planar slab configuration, where a gas layer is confined between two nonadiabatic walls conducting fixed and equal normal heat fluxes. Acoustic excitation is then imposed through added harmonic (mechanical or thermal) actuation at one of the walls. Although simple to formulate, the problem is not amenable to an exact solution, even in the linearized regime of small-amplitude excitation. Focusing on continuum-limit conditions, we subsequently derive an approximate solution based on asymptotic expansion of the acoustic fields. The limit of high-frequency actuations (yet small compared with the kinetic mean collision frequency) and slab sizes much larger than the molecular mean free path (yet vanishingly small compared to atmospheric scales, thus rendering the effect of gravity negligible) is considered. At these conditions, we find that the acoustic response is confined to a gas layer much thinner than the slab width. While a narrow layer response was also reported in previous high-frequency analyses of the adiabatic problem [9,15], the present results differ in describing the leading-order effects of system nonadiabaticity on sound propagation, which considerably modify both wave attenuation and phase speed. Applying the direct simulation Monte Carlo (DSMC) method for validation, it is shown that for small enough Knudsen numbers [$\mathrm{Kn} \lesssim O(10^{-3})$] there exists a range of frequencies,

expanding with declining Kn, where the asymptotic limit of a thin acoustic layer holds. In cases in which thermoacoustic wall excitation is applied, an ever thinner thermal layer is formed and analyzed, to describe the process of wall heat transfer into sound-wave propagation.

In view of the above, the novelty of the present contribution is in analyzing the propagation of sound in cases in which the gas maintains arbitrarily large temperature and density gradients at its reference steady state. We quantify the effect of reference state nonuniformities on high-frequency sound propagation at near-continuum conditions by obtaining closed-form expressions for the affected wave attenuation and phase speed, and demonstrating their marked differences from counterpart results at uniform reference conditions. Additionally, we analyze the particular impact of gas molecular (repulsion point center) interaction law on sound characteristics. This effect is found trivial at adiabatic reference conditions, and was therefore not considered previously.

The outline of the work is as follows. In the next section, the model problem is formulated for both vibroacoustic and thermoacoustic wall excitations. The asymptotic expansion in the limit of a thin acoustic layer is introduced and analyzed in Sec. III, followed by a description of the numerical DSMC scheme in Sec. IV. The results, highlighting the effects of problem parameters and the gas kinetic model of interaction on sound propagation, are presented in Sec. V. Concluding comments are given in Sec. VI.

II. PROBLEM STATEMENT

Consider a layer of a monatomic ideal gas of mean density ρ_m^* confined between parallel infinitely long heat-conducting walls placed at $x^* = 0$ and $x^* = L^*$ (hereafter asterisks denote dimensional quantities). The gas is heated with a constant normal heat flux at the solid surfaces,

$$\mathbf{Q}_w^{*(0)}(0) = \mathbf{Q}_w^{*(0)}(L^*) = Q_w^{*(0)}\hat{\mathbf{x}}, \tag{1}$$

where $\hat{\mathbf{x}}$ marks a unit vector in the positive x-direction. Consequently, fixed nominal hot- (T_h^*) and cold- (T_c^*) wall temperatures are maintained, and steady temperature and density distributions, $T^{*(0)}(x^*)$ and $\rho^{*(0)}(x^*)$, respectively, prevail. Starting at time $t^* = 0$, harmonic normal velocity and heat-flux excitations are imposed at the $x^* = 0$ boundary,

$$\mathbf{U}_w^*(0, t^* \geqslant 0) = \varepsilon \overline{U}_w^{*(1)} \cos(\omega^* t^*)\hat{\mathbf{x}} \quad \text{and} \quad \mathbf{Q}_w^*(0, t^* \geqslant 0) = \left[Q_w^{*(0)} + \varepsilon \overline{Q}_w^{*(1)} \cos(\omega^* t^*)\right]\hat{\mathbf{x}}, \tag{2}$$

respectively, whereas the $x^* = L^*$ surface is maintained unperturbed. In Eq. (2), $\varepsilon \ll 1$, so that the system description may be linearized about its initial state. We consider cases in which $Q_w^{(0)*} > 0$ or $Q_w^{(0)*} < 0$, for which the actuated $x^* = 0$ boundary is either the hot or cold wall, respectively, and we study the system's long-time periodic response.

A nondimensional formulation of the problem is obtained by normalizing the density by the mean density ρ_m^*, and the temperature by the nominal cold-wall temperature T_c^*. The position and velocity are scaled by L^* and $U_{\text{th}}^* = \sqrt{2\mathcal{R}^* T_c^*}$ (marking the most probable thermal speed of the gas molecules at the cold-wall temperature, with $\mathcal{R}^*$ denoting the specific gas constant), respectively, and the time is normalized by the consequent acoustic time scale, L^*/U_{th}^*. The gas pressure and stresses are nondimensionalized by $\rho_m^* U_{\text{th}}^{*2}$, and the normal heat flux is scaled by $\rho_m^* U_{\text{th}}^{*3}$. The problem is then governed by the nondimensional parameters

$$\text{Kn} = l_c^*/L^*, \quad \omega = \omega^* L^*/U_{\text{th}}^*, \quad \text{and} \quad R_T = T_h^*/T_c^*, \tag{3}$$

marking the gas Knudsen number, the scaled excitation frequency, and the walls' nominal temperatures ratio, respectively. For convenience, the introduction of the walls' temperatures ratio R_T replaces $Q_w^{(0)} = Q_w^{(0)*}/\rho_m^* U_{\text{th}}^{*3}$ as a governing parameter, and the equivalence of the two is clarified below [see Eq. (10) et seq.]. In the definition of the Knudsen number, l_c^* denotes the molecular mean free path at the cold-wall temperature, specified after Eq. (4).

Focusing on the continuum limit of slight rarefaction effects, we consider the problem for $\text{Kn} \ll 1$ and $\omega \text{Kn} \ll 1$, for which the system length scale L^* and time scale $1/\omega^*$ are large compared with the gas mean free path l_c^* and mean free time l_c^*/U_{th}^*, respectively. Adopting the

Navier-Stokes-Fourier model for a monatomic gas, the nominal gas state then satisfies the heat conduction equation

$$\frac{dq^{(0)}}{dx} = -\frac{15}{8}\text{Kn}\frac{d}{dx}\left(\mu^{(0)}\frac{dT^{(0)}}{dx}\right) = 0, \tag{4}$$

where $q^{(0)}(x)$ and $\mu^{(0)}(x)$ denote the reference distributions of gas normal heat flux and dynamic viscosity, respectively. The Knudsen number here takes the form

$$\text{Kn} = \frac{\mu_c^*}{\rho_m^* U_{\text{th}}^* L^*},$$

where μ_c^* denotes the gas viscosity at the cold-wall temperature. Combining with the definition in Eq. (3), this yields

$$l_c^* = \mu_c^*/\rho_m^* U_{\text{th}}^*$$

for the viscosity-based molecular mean free path at the cold-wall temperature. We consider an inverse power law (repulsion point center) model of molecular interaction [35], for which

$$\mu^{(0)} = (T^{(0)})^{(n+1)/2}, \tag{5}$$

where the $n = 0$ and $n = 1$ limit cases correspond to hard-sphere and Maxwell types of interaction, respectively. Applying Eq. (1) in its scaled form into Eq. (4), we find

$$q^{(0)} = \text{const} = Q_w^{(0)}. \tag{6}$$

Assigning Eq. (5) into Eq. (4), we obtain

$$\frac{d^2[(T^{(0)})^{(n+3)/2}]}{dx^2} = 0, \tag{7}$$

yielding

$$T^{(0)}(x) = (Ax + B)^{2/(n+3)}, \tag{8}$$

previously derived in Ref. [36] for a hard-sphere gas, and in Refs. [37,38] for a general power-law model of interaction. The constants A and B in Eq. (8) are determined via the imposition of the walls' temperature-jump conditions, with the temperature-jump coefficient generally depending on the type of molecular interaction [35]. Focusing on the limit of vanishingly small Knudsen numbers, we neglect this effect, and apply continuum no-jump conditions. For a setup where the hot wall is located at $x = 0$ [$T(0) = R_T, Q_w^{(0)} > 0$], we find

$$A = 1 - R_T^{(n+3)/2} \quad \text{and} \quad B = R_T^{(n+3)/2}, \tag{9}$$

whereas for an actuated cold-wall configuration [$T(0) = 1, Q_w^{(0)} < 0$]

$$A = R_T^{(n+3)/2} - 1 \quad \text{and} \quad B = 1. \tag{10}$$

The values of A and B could be equivalently expressed in terms of the walls' reference heat flux $Q_w^{(0)}$ and the total amount of energy conserved within the system, yet the present formulation is preferred for convenience. The validity of the no-jump approximation made will be tested in Sec. V, where a comparison with numerical DSMC calculations is carried out. For generality, all subsequent results are expressed in terms of A and B, without substituting their specific values in Eqs. (9) or (10), which could be easily amended to account for the (presently negligible) effect of the walls' temperature jump.

Making use of the equilibrium momentum balance in the x-direction,

$$dp^{(0)}/dx = 0,$$

it is seen that the reference pressure $p^{(0)}$ is constant across the slab, with its value fixed by the scaled form of the gas equation of state,

$$\rho^{(0)}(x) = 2p^{(0)}/T^{(0)}(x),\tag{11}$$

and a mass normalization condition,

$$\int_0^1 \rho^{(0)}dx = 1.\tag{12}$$

Substitution of Eq. (11) together with Eq. (8) into Eq. (12) yields

$$p^{(0)} = \frac{A(n+1)}{2(n+3)\left[(A+B)^{(n+1)/(n+3)} - B^{(n+1)/(n+3)}\right]},\tag{13}$$

which degenerates into the $p_{\text{iso}}^{(0)} = 1/2$ value at adiabatic ($A = 0, B = 1$) conditions. Having determined the gas reference state, we turn in the next section to analyze the acoustic field generated by the mechanical and thermal excitations imposed in Eq. (2) at the $x = 0$ wall.

III. ANALYSIS

Assuming continuum-limit conditions, the acoustic ε-order problem is governed by the one-dimensional (x-dependent) linearized Navier-Stokes-Fourier equations for a perfect monatomic gas. Focusing on the case of sinusoidal excitations specified in Eq. (2), we assume a harmonic time dependence of all hydrodynamic perturbations,

$$\Phi^{(1)}(x, t) = \text{Re}\{\overline{\Phi}^{(1)}(x)\exp(i\omega t)\},\tag{14}$$

where $\Phi^{(1)} = \{\rho^{(1)}, u^{(1)}, p^{(1)}, T^{(1)}\}$. The $O(\varepsilon)$ balances of continuity, x-momentum, and energy are then given by

$$i\omega\overline{\rho}^{(1)} + \frac{d}{dx}(\rho^{(0)}\overline{u}^{(1)}) = 0,\tag{15}$$

$$i\omega\rho^{(0)}\overline{u}^{(1)} = -\frac{d\overline{p}^{(1)}}{dx} + \frac{4}{3}\text{Kn}\frac{d}{dx}\left[(T^{(0)})^{(n+1)/2}\frac{d\overline{u}^{(1)}}{dx}\right],\tag{16}$$

and

$$i\omega\rho^{(0)}\overline{T}^{(1)} + \rho^{(0)}\frac{dT^{(0)}}{dx}\overline{u}^{(1)} = -\frac{4p^{(0)}}{3}\frac{d\overline{u}^{(1)}}{dx} + \frac{5}{2}\text{Kn}\frac{d}{dx}\left[(T^{(0)})^{(n+1)/2}\frac{d\overline{T}^{(1)}}{dx}\right],\tag{17}$$

respectively, and they are supplemented by the linearized form of the gas equation of state,

$$\overline{p}^{(1)} = \frac{1}{2}(T^{(0)}\overline{\rho}^{(1)} + \rho^{(0)}\overline{T}^{(1)}).\tag{18}$$

The system of equations is subject to a set of wall impermeability,

$$\overline{u}^{(1)}(0) = \overline{U}_w^{(1)}, \quad \overline{u}^{(1)}(1) = 0,\tag{19}$$

and heat flux,

$$\overline{q}^{(1)}(0) = \overline{Q}_w^{(1)}, \quad \overline{q}^{(1)}(1) = 0,\tag{20}$$

boundary conditions, where, in accordance with the Fourier law,

$$\overline{q}^{(1)}(x) = -\frac{15}{8}\text{Kn}\left(\mu^{(0)}\frac{d\overline{T}^{(1)}}{dx} + \overline{u}^{(1)}\frac{dT^{(0)}}{dx}\right),\tag{21}$$

and $\overline{\mu}^{(1)} = (n+1)(T^{(0)})^{\frac{n-1}{2}} \overline{T}^{(1)}/2$. Notably, by applying the viscosity-based definition of the gas mean free path [see Eq. (4) *et seq.*], the Knudsen number introduced in Eq. (3) becomes identical for all types of molecular interactions considered, and the continuum-limit formulation of the acoustic problem becomes unaffected at adiabatic reference conditions [see the above Eqs. (15)–(21) with $\rho^{(0)} = T^{(0)} = 1$]. Hence, the impact of the gas kinetic model of interaction on sound propagation in the adiabatic reference setup is found trivial. In marked difference, it is only when considering sound propagation through nonuniform reference states that the kinetic model of interaction affects the near-continuum description nontrivially, as manifested through the interaction power n [see Eq. (5)] appearing in the above $O(\varepsilon)$ balances, both explicitly and implicitly in expressions (8), (11), and (13) for $T^{(0)}$, $\rho^{(0)}$, and $p^{(0)}$, respectively. As demonstrated in the analysis below and illustrated in Sec. V, this affects the outcome attenuation rate of the acoustic signal.

While not amenable to a closed-form solution, the above problem may be solved numerically by applying finite-difference (Chebyshev-based) evaluations to the field derivatives. Such a calculation was carried out to validate the asymptotic analysis below, in addition to DSMC computations. Different from the asymptotic scheme, the formulation (15)–(21) should be valid in any case in which the continuum-limit assumptions (Kn $\ll 1$, ωKn $\ll 1$) are met, including parameter combinations where acoustic wave reflections from the unperturbed $x = 1$ wall are significant. These scenarios are, however, outside the scope of the present investigation, which focuses on the propagation of sound in the presence of a reference temperature gradient, yet in an effective "semi-infinite" domain.

A. Acoustic layer

Previous continuum-limit analyses of sound-wave propagation across uniform (initially isothermal) gas layers have indicated an exponential decay of the acoustic fields in the form [8,9,11,39–41]

$$\overline{\Phi}_{\text{iso}}^{(1)\text{AL}} \sim \exp\left[-\sqrt{\frac{6}{5}}\left(i\omega + \frac{7}{5}\omega^2 \text{Kn} \right) x \right], \tag{22}$$

showing that the acoustic disturbance is effectively confined to an acoustic layer (AL) of width $\sim O(\omega^2 \text{Kn})^{-1}$. To avoid the effect of back reflections from the unperturbed boundary, we therefore focus on a case in which $\omega^2 \text{Kn} \gg 1$, i.e., $\omega \gg \text{Kn}^{-1/2}$, for which an inner asymptotic layer expansion may be carried out. Combining with the continuum-limit restrictions on the system length scale (Kn $\ll 1$) and time scale (ωKn $\ll 1$), this confines the interval of frequencies,

$$\text{Kn}^{-1/2} \ll \omega \ll \text{Kn}^{-1}, \tag{23}$$

to be considered hereafter. With decreasing Kn $\ll 1$, the extent of this interval increases, and the analysis applies to a wider range of higher ω values.

Recalling previous analyses on high-frequency sound propagation at adiabatic reference conditions [17,40,41], the choice of the walls' separation distance L^* as the governing length scale [see Eq. (3)] may seem inappropriate, as the signal is effectively confined to a thin layer in the vicinity of the source boundary. Indeed, the relevant length scale governing the adiabatic-state problem, apart from the gas mean free path l_c^*, would be the acoustic wavelength $\lambda^* = U_{\text{th}}^*/\omega^*$. Using these scales, the acoustic field in Eq. (22) may be rewritten as

$$\overline{\Phi}_{\text{iso}}^{(1)\text{AL}} \sim \exp\left[-\sqrt{\frac{6}{5}}\left(i + \frac{7}{5}\frac{l_c^*}{\lambda^*} \right) \frac{x^*}{\lambda^*} \right],$$

revealing the wavelength-based Knudsen number l_c^*/λ^* as the single nondimensional parameter governing the propagation of sound at adiabatic reference conditions. Having noted that, and in marked contrast, the walls' distance L^* does become relevant in the nonadiabatic problem, measuring the characteristic length over which the steady reference fields vary. In this case, the

source-induced perturbations, even if confined to a thin layer, are propagating through an effective semi-infinite domain characterized by $O(1/L^*)$ gradients of the hydrodynamic quantities $T^{*(0)}(x^*)$ and $\rho^{*(0)}(x^*)$. The separation distance L^* in the nonadiabatic reference case then directly affects the sound propagation and attenuation rate, and its preference over λ^* as the normalizing length scale is most suitable for analysis consistency and illustration of the differences between the adiabatic and nonadiabatic problems.

Considering the nonisothermal reference state in our problem, and taking into account the adiabatic-limit result in Eq. (22), we assume a general form for the acoustic layer solution

$$\overline{\Phi}_{\text{noniso}}^{(1)\text{AL}} = \big[\widetilde{\Phi}_1(x) + i\omega\text{Kn}\widetilde{\Phi}_2(x) + (\omega\text{Kn})^2\widetilde{\Phi}_3(x) + \cdots\big]\exp\big[i\omega\big(\theta_{\Phi,1}(x) + (\omega\text{Kn})^2\theta_{\Phi,2}(x)\cdots\big)\big],$$
(24)

where $\widetilde{\Phi}_j(x)$ and $\theta_{\Phi,j}(x)$ are $O(1)$ real functions describing the wave decay rate and phase, respectively. We seek an inner acoustic-layer solution for the attenuation functions

$$\widetilde{\Phi}_j(x) = \hat{\Phi}_j(\xi),$$
(25)

where

$$\xi = (\omega^2\text{Kn})x$$
(26)

denotes the inner-layer coordinate. Assigning Eq. (24) together with Eq. (26) into Eq. (15) and differentiating yield the leading-order expression for $d\overline{\rho}^{(1)\text{AL}}/dx$,

$$\frac{d\overline{\rho}^{(1)\text{AL}}}{dx} = -i\omega\rho^{(0)}\hat{u}_1\left(\frac{d\theta_{u,1}}{dx}\right)^2.$$
(27)

A similar substitution into Eq. (17) and x-differentiation yield the leading-order balance for $d\overline{T}^{(1)\text{AL}}/dx$,

$$\frac{d\overline{T}^{(1)\text{AL}}}{dx} = -\frac{2i}{3}\omega T^{(0)}\hat{u}_1\left(\frac{d\theta_{u,1}}{dx}\right)^2.$$
(28)

Substituting Eqs. (27) and (28) into Eq. (16) in conjunction with Eqs. (11) and (18), the leading $O(\omega)$ x-momentum balance takes the form

$$\frac{d\theta_{u,1}}{dx} = \pm\sqrt{\frac{6}{5T^{(0)}}}.$$
(29)

Retaining only the negative root sign, which corresponds to a causal wave traveling in the positive x-direction, Eq. (29) is integrated. Making use of Eq. (8), and imposing a zero phase boundary condition at the wall [stemming from the impermeability condition; see Eq. (2)],

$$\theta_{u,1}(0) = 0,$$

we obtain

$$\theta_{u,1}(x) = -\sqrt{\frac{6}{5}}\frac{(n+3)}{A(n+2)}\big[(Ax+B)^{(n+2)/(n+3)} - B^{(n+2)/(n+3)}\big].$$
(30)

In accordance with Eq. (29), the local wave speed is

$$c^{(0)}(x) = \left|\left(\frac{d\theta_{u,1}}{dx}\right)^{-1}\right| = \sqrt{\frac{5T^{(0)}}{6}},$$
(31)

which, in the isothermal $T^{(0)} = 1$ case, degenerates into the scaled uniform speed of sound for a monatomic gas, $c^{(0)} = \sqrt{5/6}$. Reverting to the $O(\omega)$ balance of the energy equation (17),

$$\hat{T}_1 = -\frac{2}{3}T^{(0)}\frac{d\theta_{u,1}}{dx}\hat{u}_1,$$
(32)

and combining with Eq. (28), we obtain

$$\frac{d\theta_{T,1}}{dx} = \frac{d\theta_{u,1}}{dx} \equiv \frac{d\theta_1}{dx}, \tag{33}$$

indicating the same leading-order phase variation of the velocity and temperature perturbations.

The attenuation functions $\widetilde{\Phi}_1(x) = \hat{\Phi}_j(\xi)$ can now be evaluated using the next-order perturbation equations. Assigning Eq. (33) into Eq. (16), the $O(\omega^2 \mathrm{Kn})$ momentum balance reads

$$\frac{10}{3}p^{(0)}\left(\frac{d\theta_1}{dx}\right)\frac{d\hat{u}_1}{d\xi} - \frac{4}{3}T^{(0)}\left(\frac{d\theta_1}{dx}\right)^2 \hat{u}_1 + \frac{5}{4}T^{(0)}\left(\frac{d\theta_1}{dx}\right)^3 \hat{T}_1 + \rho^{(0)}\left[1 - \frac{5}{6}T^{(0)}\left(\frac{d\theta_1}{dx}\right)^2\right]\hat{u}_2 = 0. \tag{34}$$

Substituting Eqs. (32), (33), and (29) into Eq. (34), we arrive at the simplified form

$$\frac{d\hat{u}_1}{d\xi} + \frac{7}{10p^{(0)}}\sqrt{\frac{6(T^{(0)})^n}{5}}\hat{u}_1 = 0. \tag{35}$$

Observing Eq. (35), the effect of gas nonuniform reference conditions on the attenuation rate may be quantitated by considering the relative decay ratio

$$\mathcal{D} = \frac{(d\hat{u}_1/\hat{u}_1)_{\mathrm{noniso}}}{(d\hat{u}_1/\hat{u}_1)_{\mathrm{iso}}} = \sqrt{\frac{5}{24}}\frac{\mu^{(0)}(x)}{c^{(0)}(x)p^{(0)}} \tag{36}$$

between the relative velocity variations in the nonisothermal and isothermal configurations. Viewing Eq. (36), it is inferred that the differences in exponential attenuations between the two setups may originate from x-variations of the gas viscosity and speed of sound in the nonisothermal configuration, as well as deviations of the constant ambient pressure $p^{(0)} = p^{(0)}(R_T, n)$ from its isothermal $p^{(0)}_{\mathrm{iso}} = 1/2$ counterpart. Notably, for a hard-sphere gas [$n = 0$ in Eq. (5)], the common square-root temperature dependencies of gas viscosity and speed of sound cancel out, and the difference in attenuation is attributed only to the change in the ambient pressure. As $p^{(0)}(R_T, n = 0)$ increases monotonically with R_T [see Eq. (13) and Fig. 2(d)], sound attenuation weakens monotonically. At a given R_T, this turns out to be the weakest attenuation rate among all other ($0 \leqslant n \leqslant 1$) point-repulsion models of interaction, as the competing effects of temperature nonuniformity on gas pressure and viscosity in non-hard-sphere gases result in stronger wave decay.

Assigning $d\xi = \omega^2\mathrm{Kn}dx$ together with Eq. (8) into Eq. (35), we obtain

$$\frac{d\widetilde{u}_1}{\widetilde{u}_1} = -\frac{7}{10p^{(0)}}\sqrt{\frac{6}{5}}(Ax + B)^{n/(n+3)}\omega^2\mathrm{Kn}dx. \tag{37}$$

Integrating Eq. (37) and applying the impermeability condition in Eq. (19), we find

$$\widetilde{u}_1 = \overline{U}_w^{(1)}\exp\left[-\frac{7}{10}\sqrt{\frac{6}{5}}\frac{(n+3)}{(2n+3)}\frac{\omega^2\mathrm{Kn}}{p^{(0)}A}\left((Ax + B)^{(2n+3)/(n+3)} - B^{(2n+3)/(n+3)}\right)\right]. \tag{38}$$

Substituting Eqs. (30) and (38) for the wave phase and attenuation into Eq. (24), the leading order of the velocity field in the acoustic layer is obtained,

$$\begin{aligned}\overline{u}_{\mathrm{noniso}}^{(1)\mathrm{AL}}(x) &\approx \widetilde{u}_1(x)\exp[i\omega\theta_{u,1}(x)] \\ &= \overline{U}_w^{(1)}\exp\left[-\sqrt{\frac{6}{5}}i\omega\frac{(n+3)}{(n+2)A}\left[(Ax + B)^{(n+2)/(n+3)} - B^{(n+2)/(n+3)}\right]\right. \\ &\quad \left. -\frac{7}{10}\sqrt{\frac{6}{5}}\frac{(n+3)}{(2n+3)}\frac{\omega^2\mathrm{Kn}}{p^{(0)}A}\left((Ax + B)^{(2n+3)/(n+3)} - B^{(2n+3)/(n+3)}\right)\right]. \end{aligned} \tag{39}$$

The above expression generalizes the previously obtained phase speed and attenuation rate in the counterpart adiabatic reference problem [see Eq. (22)] to the case of a nonadiabatic setup. In line with the discussion after Eq. (23), the deviation of the nonadiabatic result from its adiabatic counterpart is characterized by functions varying over the walls' separation distance scale L^* [$\sim O(1)$ in our nondimensional formulation]. Thus, different from the adiabatic problem, the choice of L^* as the characteristic length scale here is required, and it illustrates the dissimilarities between the adiabatic and nonadiabatic system behaviors. Making use of the $O(\omega)$ energy balance in Eq. (32), the counterpart continuity equation, and the equation of state (18), the leading order for the acoustic pressure is given by

$$\overline{p}_{\text{noniso}}^{(1)\text{AL}}(x) \approx \frac{5}{3}p^{(0)}\sqrt{\frac{6}{5T^{(0)}}}\overline{u}_{\text{noniso}}^{(1)\text{AL}}(x), \tag{40}$$

indicating an equal phase yet a different attenuation rate between the velocity and pressure perturbations. Specifically, the pressure and velocity exponential attenuation is similar, but the former is further multiplied by the inverse speed of sound, which may be either an increasing ($Q_w^{(0)} > 0$) or a decreasing ($Q_w^{(0)} < 0$) function of x [see Eqs. (8)–(10)].

While the leading-order solutions for $\overline{u}_{\text{noniso}}^{(1)\text{AL}}$ and $\overline{p}_{\text{noniso}}^{(1)\text{AL}}$ satisfy the impermeability condition, the heat-flux condition in Eq. (20) should still be considered. Evaluation of the leading-order gas heat-flux perturbation at the wall yields

$$\overline{q}_{\text{noniso}}^{(1)\text{AL}}(0) = -\frac{15}{8}\text{Kn}\mu^{(0)}\frac{d\overline{T}_{\text{noniso}}^{(1)\text{AL}}}{dx}\bigg|_{x=0} \sim O(\omega\text{Kn}), $$

which, since $\omega\text{Kn} \ll 1$, cannot be directly matched with an arbitrary $O(1)$ (ε-scaled) choice of $\overline{Q}_w^{(1)}$ [see Eq. (20)]. The above acoustic layer approximation may therefore agree only with an *adiabatic* wall condition, whereas a further correction must be sought to study the thermoacoustic problem. Indeed, in terms of physical interpretation, the acoustic-layer calculation shows that the heat-flux magnitude remains $O(\omega\text{Kn}) \ll 1$ within the layer regardless of the value of $\overline{Q}_w^{(1)}$, necessitating that any wall-inserted heat is converted into compressible work and internal gas energy at a short distance from the wall. This requires the formation of a further inner *thermal layer* (TL), where, for $\overline{Q}_w^{(1)} \sim O(1)$, the conversion of heat into mechanical work yields an effective matching condition for the velocity (and hence affects the acoustic pressure) in the acoustic layer.

Reverting to the isothermal reference case, previous works have shown that a thermal layer of width $\sim O(\sqrt{\text{Kn}/\omega}) \ll (\omega^2\text{Kn})^{-1}$ (as $\omega\text{Kn} \ll 1$) forms in response to thermoacoustic wall excitation [17,40,41]. We hence follow a similar assumption in the present nonisothermal setup. Integrating the energy equation (17) over the layer and retaining the leading-order terms, we obtain an effective matching condition to complement Eq. (37),

$$\overline{u}^{(1)\text{AL}}(x \to 0) = \overline{u}^{(1)\text{TL}}(x \gg \sqrt{\text{Kn}/\omega}) = \frac{\overline{Q}_w^{(1)}}{p^{(0)}} - \frac{3i\omega}{4p^{(0)}}\int_0^{x \gg \sqrt{\text{Kn}/\omega}}\overline{T}^{(1)\text{TL}}(x)dx. \tag{41}$$

Assigning $\overline{T}^{(1)\text{TL}}(x)$ that was obtained in the isothermal reference case [17],

$$\overline{T}_{\text{iso}}^{(1)\text{TL}}(x) = -\frac{8\overline{Q}_w^{(1)}}{15\sqrt{i\omega\text{Kn}}}\exp\left[-\sqrt{\frac{2i\omega}{3\text{Kn}}}x\right], \tag{42}$$

we find

$$\overline{u}_{\text{iso}}^{(1)\text{AL}}(x \to 0) = \overline{u}_{\text{iso}}^{(1)\text{TL}}(x \gg \sqrt{\text{Kn}/\omega}) = \frac{2\overline{Q}_w^{(1)}}{5p_{\text{iso}}^{(0)}} = \frac{4\overline{Q}_w^{(1)}}{5}, \tag{43}$$

where the isothermal $p_{\text{iso}}^{(0)} = 1/2$ value has been assigned. In a setup where both mechanical and thermal excitations are imposed, the matching condition is given by the superposition

$$\overline{u}_{\text{iso}}^{(1)\text{AL}}(x \to 0) = \overline{U}_w^{(1)} + \frac{4\overline{Q}_w^{(1)}}{5}, \tag{44}$$

suggesting that a wall heat flux of $\overline{Q}_w = -5\overline{U}_w/4$ eliminates the vibroacoustic far field [17]. The next section analyzes the thermoacoustic problem in the nonisothermal reference case, where a counterpart evaluation for the optimal value of $\overline{Q}_w^{(1)}$ required for sound cancellation is obtained.

B. Thermal layer

Recalling the general form of the thermal-layer solution in the isothermal reference case [17,39–41],

$$\overline{\Phi}_{\text{iso}}^{(1)\text{TL}} \sim \exp\left[-\sqrt{\frac{2i\omega}{3\text{Kn}}}x\right], \tag{45}$$

we seek an inner-layer representation

$$\overline{\Phi}_{\text{noniso}}^{(1)\text{TL}}(x) = \check{\Phi}(\eta), \tag{46}$$

where the inner-layer coordinate

$$\eta = \sqrt{\frac{\omega}{\text{Kn}}}x \tag{47}$$

is introduced. Considering the leading order of the $x = 0$ thermal boundary condition in Eq. (20),

$$-\frac{15}{8}\text{Kn}\left[(T^{(0)})^{(n+1)/2}\frac{d\overline{T}_{\text{noniso}}^{(1)\text{TL}}}{dx}\right]_{x=0} = \overline{Q}_w^{(1)} \sim O(1), \tag{48}$$

we derive an asymptotic expansion for the temperature perturbation in the thermal layer,

$$\overline{T}_{\text{noniso}}^{(1)\text{TL}} = \frac{1}{\sqrt{\omega\text{Kn}}}\check{T}_1 + \sqrt{\omega\text{Kn}}\check{T}_2 + O(\omega\text{Kn})^{3/2}, \tag{49}$$

whereas the asymptotic scaling for the velocity is obtained from the energy balance as

$$\overline{u}_{\text{noniso}}^{(1)\text{TL}} = \check{u}_1 + (\omega\text{Kn})\check{u}_2 + O(\omega\text{Kn})^2. \tag{50}$$

A schematic of the double-layer configuration containing the gas thermal and acoustic layers is shown in Fig. 1, where the purpose of the following analysis is to obtain an effective matching condition,

$$\overline{u}_{\text{noniso}}^{(1)\text{AL}}(x \to 0) = \overline{u}_{\text{noniso}}^{(1)\text{TL}}(x \gg \sqrt{\text{Kn}/\omega}),$$

which takes into account the wall thermoacoustic excitation $\overline{Q}_w^{(1)} \neq 0$.

Assigning Eqs. (49) and (50) together with Eq. (47) into the continuity, momentum, and energy equations (15)–(17), respectively, we arrive at the leading-order balances

$$\frac{d^2\check{u}_1}{d\eta^2} = \frac{3(T^{(0)})^{(n+1)/2}}{4p^{(0)}}\frac{d^3\check{T}_1}{d\eta^3} \tag{51}$$

and

$$\frac{d\check{u}_1}{d\eta} = \frac{15(T^{(0)})^{(n+1)/2}}{8p^{(0)}}\frac{d^2\check{T}_1}{d\eta^2} - \frac{3i}{2T^{(0)}}\check{T}_1. \tag{52}$$
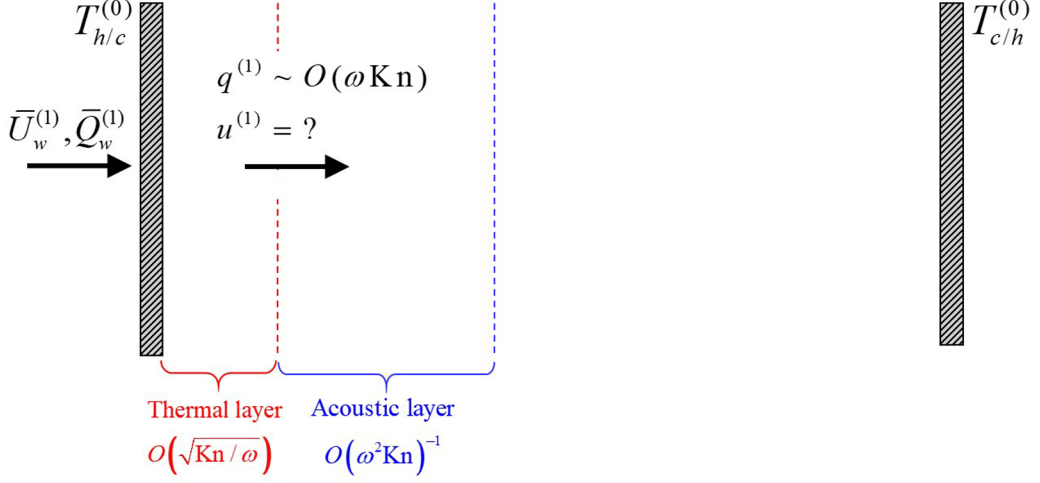
FIG. 1. Schematic of the double-layer configuration containing the gas thermal and acoustic layers. The parameters $\text{Kn} \ll 1$ and $\omega \gg 1$ considered are chosen such that the layers are asymptotically thin compared with the unity slab width.

Combining Eqs. (51) and (52) together with Eq. (8) and introducing

$$\overline{\tau}_{\text{noniso}}^{(1)\text{TL}}(x) = \text{Kn} \frac{d\overline{T}_{\text{noniso}}^{(1)\text{TL}}}{dx},$$

we obtain the relations

$$\frac{d^2\overline{\tau}_{\text{noniso}}^{(1)\text{TL}}}{dx^2} - \frac{4i\omega}{3\text{Kn}} \frac{p^{(0)}}{(Ax+B)} \overline{\tau}_{\text{noniso}}^{(1)\text{TL}} = 0 \tag{53}$$

and

$$\frac{d^2\overline{u}_{\text{noniso}}^{(1)\text{TL}}}{dx^2} = \frac{3}{4p^{(0)}}(Ax+B)^{(n+1)/(n+3)}\frac{d^2\overline{\tau}_{\text{noniso}}^{(1)\text{TL}}}{dx^2}. \tag{54}$$

The decoupled Eq. (53) for $\overline{\tau}_{\text{noniso}}^{(1)\text{TL}}$, subject to wall heat flux and far-field decay conditions, may be solved in a closed form. Following the calculation in the Appendix, this yields

$$\overline{\tau}_{\text{noniso}}^{(1)\text{TL}}(x) = -\frac{8\overline{Q}_w^{(1)}}{15} \frac{\sqrt{Ax+B}}{B^{(3n+5)/2(n+3)}} \frac{Y_1\left(\frac{4}{A}\sqrt{\frac{\omega p^{(0)}}{3i\text{Kn}}(Ax+B)}\right)}{Y_1\left(\frac{4}{A}\sqrt{\frac{\omega p^{(0)}B}{3i\text{Kn}}}\right)}, \tag{55}$$

where $Y_1(\cdot)$ is the first-order Bessel function of the second kind. We now substitute Eq. (55) into Eq. (54) and integrate twice. Evaluating the result at $x \gg \sqrt{\text{Kn}/\omega}$ and retaining the $O(1)$ leading-order term, we obtain the desired matching condition

$$\overline{u}_{\text{noniso}}^{(1)\text{AL}}(x \to 0) = \overline{u}_{\text{noniso}}^{(1)\text{TL}}(x \gg \sqrt{\text{Kn}/\omega}) = \frac{2\overline{Q}_w^{(1)}}{5p_{\text{noniso}}^{(0)}} + O(\sqrt{\text{Kn}/\omega}). \tag{56}$$

Comparing between Eqs. (56) and (43), we find that the isothermal and nonisothermal setups differ by replacing the isothermal $p_{\text{iso}}^{(0)} = 1/2$ with $p_{\text{noniso}}^{(0)} = p_{\text{noniso}}^{(0)}(R_T, n)$, respectively. Considering a case in which both mechanical and thermal excitations are applied, the combined matching

condition reads

$$\overline{u}_{\mathrm{iso}}^{(1)\mathrm{AL}}(x \to 0) = \overline{U}_w^{(1)} + \frac{2\overline{Q}_w^{(1)}}{5p_{\mathrm{noniso}}^{(0)}}. \tag{57}$$

The solution for the acoustic field is consequently obtained through replacing $\overline{U}_w^{(1)}$ in Eq. (38) by the right-hand side in Eq. (57). Optimal far-field vibroacoustic sound cancellation is therefore achieved by taking

$$\overline{Q}_w^{(1)} = -\frac{5}{2}p^{(0)}(R_T, n)\overline{U}_w^{(1)}, \tag{58}$$

which degenerates into the isothermal-setup result,

$$\overline{Q}_w = -5\overline{U}_w/4,$$

for $R_T = 1$ [see Eq. (44) *et seq.*].

IV. NUMERICAL SCHEME: DSMC METHOD

The DSMC method, initially proposed by Bird, is a stochastic particle method commonly applied for the analysis of gas flows at noncontinuum conditions [42]. In this context, application of the method to the present problem may seem inefficient, noting the vanishingly small global (slab-width-based) Knudsen numbers considered (see Sec. V). Yet, the imposition of large excitation frequencies leads to the formation of thin acoustic layers, where nonsmall rarefaction effects prevail. At these conditions, the applicability of the continuum description should be validated, for which the DSMC scheme is used. By doing so, the system acoustic response is calculated independently to confirm the continuum-limit-based solutions presented in Sec. III.

We therefore adopt Bird's algorithm, together with the variable hard-sphere (VHS) model of molecular interaction [42], to simulate the gas state. To enable a comparison between the DSMC and continuum solutions for Maxwell and hard-sphere molecules, the molecular collision cross section is defined accordingly, as detailed in Ref. [41]. Complying with the problem formulation, the boundaries are modeled as fully diffuse and with a prescribed heat flux. To apply the latter, the boundary temperature is treated as unknown, and a modification of the conventional computational scheme is required. This is carried out using recent contributions by the authors [40,41,43,44], where a noniterative algorithm for the imposition of a heat-flux condition has been described and tested.

At the vanishingly small ($\lesssim 10^{-3}$) Knudsen numbers considered in this work, DSMC calculations might become considerably time-consuming, even for the relatively short ($\propto \omega^{-1}$) flow time scales studied. To overcome this difficulty, we capitalized on the thinness of the affected layer to reduce the computational domain. This was achieved by replacing the actual $x = 1$ far wall with a "virtual" closer wall, positioned at a point where the acoustic perturbations effectively vanish. The effective computational domain was then divided into 200 cells, with an additional division of each cell into collisional subcells of width $l_c^*/4$ taken to comply with the mean free path limitations. The magnitude of the time increment was consequently set to $l_c^*/(4U_{\mathrm{th}}^*)$. For the harmonic wall excitation studied in this work, the computation was followed until the system had reached its final periodic state. A typical run consisted of $\approx 3 \times 10^7$ particles, where 16 realizations were carried out simultaneously to sufficiently reduce the numerical noise. Each simulation lasted several hours using a ten-core Intel i7-6950 machine.

V. RESULTS

We now turn to illustrate the effect of system nonadiabaticity on acoustic wave propagation. To this end, we fix $R_T = 2$ for the nonadiabatic state calculations (apart from Figs. 2 and 4, where the effect of varying R_T is examined), and compare our findings with a reference adiabatic $R_T = 1$ case. In the nonadiabatic setups, we consider configurations where the hot wall is acoustically perturbed,
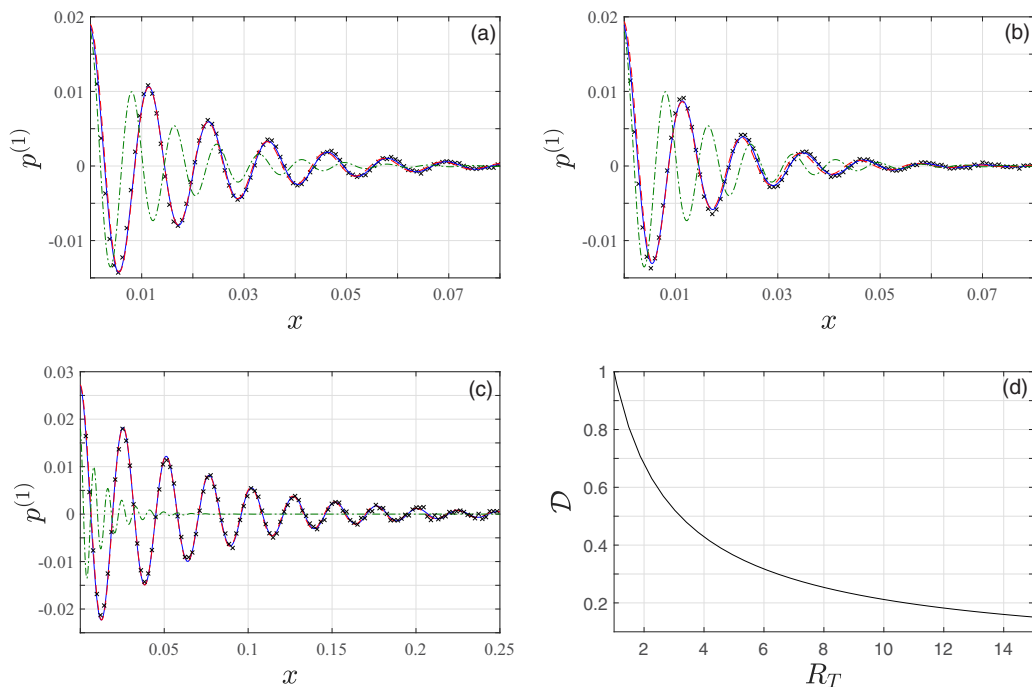
FIG. 2. (a)–(c) Variation with x of the acoustic pressure generated by vibroacoustic ($\overline{U}_w^{(1)} = 0.02$, $\overline{Q}_w^{(1)} = 0$) wall excitation for (a), (c) hard-sphere ($n = 0$) and (b) Maxwell-type ($n = 1$) gas with Kn $= 10^{-4}$, $\omega = 700$ and (a,b) $R_T = 2$; (c) $R_T = 10$. The solid blue lines, dashed red curves, and black crosses present finite-difference-based, asymptotic, and DSMC results, respectively, whereas the dash-dotted green curves depict the reference adiabatic ($R_T = 1$) signal. All results are presented at period time, $t = 2\pi/\omega$. (d) Variation with R_T of the relative decay ratio $\mathcal{D}$ [see Eq. (36)] for a hard-sphere gas.

thus located at $x = 0$. In a single case (see Fig. 4), a configuration where the cold wall is actuated is examined. We choose parameter combinations of Kn and ω that agree with both continuum-limit (Kn $\ll 1$, ωKn $\ll 1$) and asymptotic-limit ($\omega \gg$ Kn$^{-1/2}$) assumptions, and examine the impact of the gas kinetic law of interaction by comparing between the extremal rigid sphere ($n = 0$) and Maxwell ($n = 1$) molecules setups. The continuum-limit-based results are validated through comparison with DSMC calculations to support our findings. For convenience, the gas responses to vibroacoustic and thermoacoustic wall excitations are discussed separately in Secs. V A and V B, respectively.

A. Vibroacoustic wave propagation

Starting with the case of hot-wall vibroacoustic excitation, we set $\overline{U}_w^{(1)} = 0.02$ and $\overline{Q}_w^{(1)} = 0$ in Eqs. (19) and (20). Figures 2(a)–2(c) then present respective x-variations of the acoustic pressure $p^{(1)}$ at period time, comparing between finite-difference-based (solid blue lines), asymptotic (dashed red curves), and DSMC (crosses) results for Kn $= 10^{-4}$ and $\omega = 700$. The (Kn, ω) combination is chosen such that the condition (23) is satisfied, and a comparison is made between the results for hard-sphere- [Figs. 2(a) and 2(c)] and Maxwell- [Fig. 2(b)] type gases. In Figs. 2(a) and 2(b), the results are presented for $R_T = 2$, whereas in Fig. 2(c) $R_T = 10$. The agreement between the solutions is very good in all cases, supporting the accurateness of the analysis. The direct effect of system nonadiabaticity is illustrated through a comparison with the adiabatic ($R_T = 1$) signal at

the same (Kn, ω) combination. For easy reference, Fig. 2(d) shows the hard-sphere x-independent variation of the relative decay ratio $\mathcal{D}$ with R_T [see Eq. (36) with $n = 0$], given by $\mathcal{D} = 1/(2p^{(0)})$.

Focusing on Figs. 2(a) and 2(b) and inspecting the gas layer affected by the wall excitation, we observe that the acoustic field extends through $x \lesssim 0.08$. This is in order-of-magnitude accordance with our acoustic-layer estimates, predicting a layer of width $\sim O(\omega^2 \text{Kn})^{-1}$. The attenuation rate is seen to be stronger for a Maxwell gas and weaker for a hard-sphere gas, with both signals extending further away from the wall compared with the adiabatic wave. This agrees with the discussion in Sec. III A [see Eq. (36) et seq.], predicting the weakest decay rate (and thus furthest extension) of the signal in the hard-sphere case. The phases in the nonadiabatic configurations precede the adiabatic-signal counterpart due to a larger local speed of sound in the vicinity of the $x = 0$ hot wall [see Eq. (31)]. No visible phase differences are observed between the two nonadiabatic signals, as the speed of sound in this limit is a function of the temperature only, being $\approx R_T$ (approximately n-independent) near the wall [see Eqs. (8) and (9)].

Traversing to Fig. 2(c) and comparing with Fig. 2(a), we first observe the significant effect of increasing R_T (from $R_T = 2$ to 10) on the departure between the nonadiabatic and adiabatic signals, and the considerable extension of the acoustic layer in the former. Indeed, apart from the $O(\omega^2 \text{Kn})^{-1}$ asymptotic estimate for the layer size, a closer inspection of the results in Sec. III A reveals the dependence of the layer width on R_T. Focusing on the exponential decay found in Eq. (39) and taking $n = 0$ for a hard-sphere gas, we find the estimate

$$\overline{\Phi}_{\text{noniso}}^{(1)\text{AL}} \sim \exp\left[-\frac{7}{5}\sqrt{\frac{6}{5}}\frac{\omega^2 \text{Kn}}{2p^{(0)}}x \right] \tag{59}$$

for the exponentially attenuating part of the nonadiabatic solution. Comparing with the adiabatic decay rate recalled in Eq. (59), the difference in attenuation between the signals is then attributed to the $\mathcal{D} = 1/2p^{(0)}$ ratio deviation. To clarify its effect, Fig. 2(d) plots the dependence of $\mathcal{D}$ on R_T, supporting a monotonic reduction in attenuation with increasing system nonadiabaticity. Clearly, with the increase in the reference wall heating $Q_w^{(0)}$, $p^{(0)}$ becomes larger, resulting in the effective propagation of sound over larger distances. A qualitatively similar conclusion (yet more cumbersome in detail) arises when considering different non-hard-sphere ($0 < n \leqslant 1$) models of interaction.

To further assess the validity of the AL solution, Fig. 3 compares between the ω-variations of the extremal acoustic pressure adjacent to the $x = 0$ wall, noted $p_{\text{ext}}^{(1)}$, as predicted by the finite-difference (solid blue line) and asymptotic (dashed red curve) calculations. A hard-sphere gas with $R_T = 2$ is considered, the Knudsen number $\text{Kn} = 10^{-4}$ is fixed, and the results are plotted at period $t = 2\pi/\omega$ time. As a reference, the value of $p_{\text{ext}}^{(1)} \approx -0.014$ obtained at $\omega = 700$ matches with the respective extremal value of $p^{(1)}$ presented in Fig. 2(a) closest to the wall.

In accordance with Eq. (23) and the value of Kn considered, the asymptotic scheme should be valid for $10^2 \ll \omega \ll 10^4$. This is supported by the results in Fig. 3, showing deviations between the dashed and solid lines for $\omega \lesssim 200$ and $\omega \gtrsim 10^3$. Notably, the low- and high-frequency breakdowns of the asymptotic solution are attributed to different mechanisms: for $\omega \sim O(\text{Kn}^{-1}) = O(10^4)$, the acoustic layer becomes of similar width to that of the Knudsen layer, leading to the breakdown of the continuum-limit assumption, and to inaccuracies in both asymptotic and finite-difference continuum-based solutions. In contrast, for $\omega \sim O(\text{Kn}^{-1/2}) = O(10^2)$, only the asymptotic scheme turns inconsistent, as the estimated layer width [$\sim(\omega^2 \text{Kn})^{-1}$] becomes $O(1)$, and the effect of waves reflection at the $x = 1$ wall becomes dominant. Indeed, the backreflection of waves at the far wall is the cause of the fluctuations observed in the finite-difference solution for $\omega \lesssim 200$. This effect could not be captured by the asymptotic calculation, which assumes wave propagation through an effectively semi-infinite domain.

To conclude the discussion on vibroacoustic wave propagation, we examine the case of cold-wall excitation in Fig. 4, where $T^{(0)}(x = 0) = 1$ and $T^{(0)}(x = 1) = R_T$. For easy reference, the same parameter values of $\overline{U}_w^{(1)} = 0.02$, $\omega = 700$, and $\text{Kn} = 10^{-4}$ are taken as in Fig. 2, and the
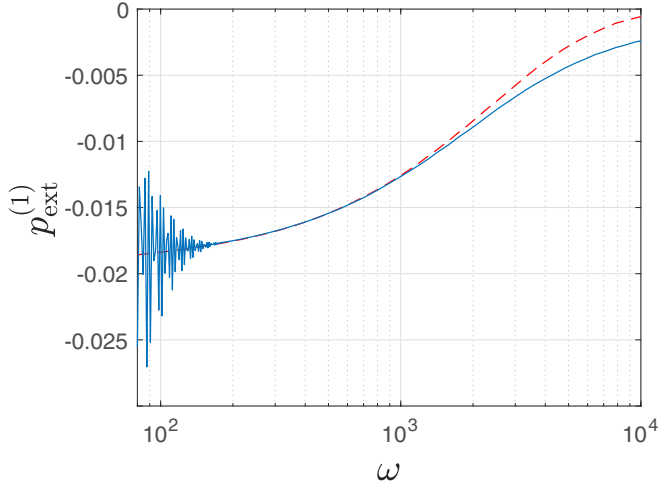
FIG. 3. Validity of the asymptotic solution for a hard-sphere gas at $R_T = 2$ and $\text{Kn} = 10^{-4}$ subject to vibroacoustic ($\overline{U}_w^{(1)} = 0.02$, $\overline{Q}_w^{(1)} = 0$) wall excitation: variations with ω of the extremal acoustic pressure adjacent to the $x = 0$ wall at time $t = 2\pi/\omega$, as predicted by the finite-difference (solid blue line) and asymptotic (dashed red curve) calculations.

x-variations of the acoustic pressure $p^{(1)}$ for Maxwell molecules ($n = 1$) at period time are presented. In Figs. 4(a) and 4(b), the results for $R_T = 2$ and 10 are shown, respectively. The reference adiabatic ($R_T = 1$) signal, appearing as green dashed-dotted lines, is identical with the one presented in Fig. 2.

Overall, the considerable effect of the reference-state gradient in extending the acoustic wave penetration depth is observed, in common with the hot-wall excitation response. Nevertheless, comparing with the results in Fig. 2, some differences are found. At first, in contrast with Fig. 2, the signals in Fig. 4 occur in phase with the adiabatic signal in the vicinity of the wall, as imposed by their $x = 0$ common cold-wall temperature. The phase lead of the nonadiabatic signal is then achieved with increasing distance from the boundary due to the temperature gradient. Additionally,
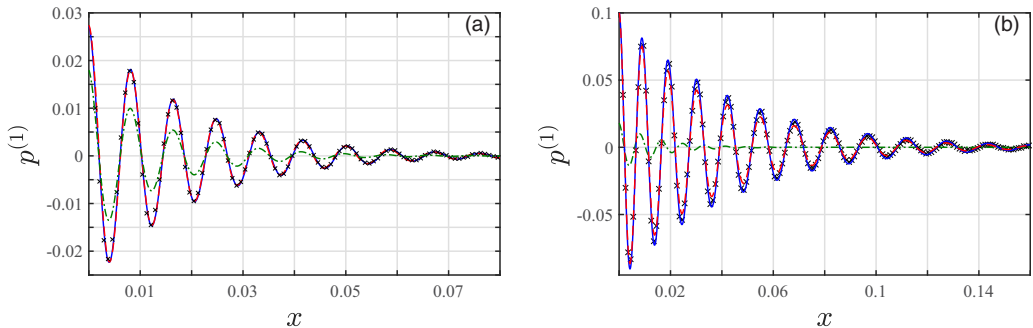

FIG. 4. Variation with x of the acoustic pressure generated by vibroacoustic ($\overline{U}_w^{(1)} = 0.02$, $\overline{Q}_w^{(1)} = 0$) wall excitation for a Maxwell-type ($n = 1$) gas with $\text{Kn} = 10^{-4}$, $\omega = 700$, and (a) $R_T = 2$; (b) $R_T = 10$. The solid blue lines, dashed red curves, and black crosses present finite-difference-based, asymptotic, and DSMC results, respectively, whereas the dash-dotted green curves depict the reference adiabatic ($R_T = 1$) signal. All results are presented at period time, $t = 2\pi/\omega$. Different from Figs. 2 and 3 and the next figures, the heated wall is located at $x = 1$, whereas the actuated $x = 0$ boundary is set at the reference temperature $T^{(0)} = 1$.
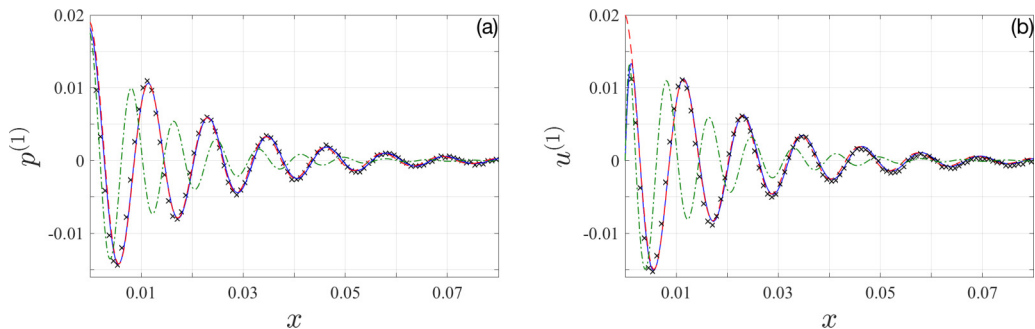
FIG. 5. Variation with x of the (a) acoustic pressure and (b) velocity perturbation generated by thermoacoustic ($\overline{U}_w^{(1)} = 0$, $\overline{Q}_w^{(1)} = 0.02 \times 5p^{(0)}/2$) wall excitation for a hard-sphere gas with $R_T = 2$, Kn $= 10^{-4}$, and $\omega = 700$. The solid blue lines, dashed red curves, and black crosses present finite-difference-based, asymptotic, and DSMC results, respectively, whereas the dash-dotted green curves present the reference adiabatic ($R_T = 1$) signal. All results are presented at period time, $t = 2\pi/\omega$.

we observe that the pressure wave amplitude is larger in the case of cold-wall excitation [cf. Figs. 4(a) and 2(b)]. Inspecting the order of magnitude of the acoustic pressure obtained in Eq. (40),

$$\overline{p}_{\text{noniso}}^{(1)\text{AL}}(x) \sim \frac{p^{(0)}}{\sqrt{T^{(0)}}} \overline{U}_w^{(1)},$$

this difference is attributed to the increase in the reference ambient pressure (relative to the adiabatic case), accompanied by the "local" cold temperature conditions in the vicinity of the actuated wall. This trend is especially noticeable for $R_T = 10$ [see Fig. 4(b)], where it leads to a slight disagreement between the asymptotic and numerical (finite-difference and DSMC) solutions. Indeed, at such large imposed temperature gradients and consequent large pressure fluctuations, the assumption made in the asymptotic scheme that all the acoustic fields are of the same order [see Eq. (24)] is only partially satisfied, hence leading to the observed discrepancies.

B. Thermoacoustic wave propagation

Considering the system response to thermoacoustic wall excitation, Fig. 5 presents x-variations of the acoustic pressure [Fig. 5(a)] and velocity perturbation [Fig. 5(b)] for a hard-sphere gas in response to boundary actuation at $\overline{Q}_w^{(1)} = 0.02 \times 5p^{(0)}/2$ and $\overline{U}_w^{(1)} = 0$ [see Eqs. (19) and (20)]. For easy reference, the (Kn, ω) = $(10^{-4}, 700)$ combination is chosen as in Fig. 2. Good agreement is found between the asymptotic, finite-difference, and DSMC solutions, reconfirming the correctness of the continuum-limit calculations at the relatively high frequency taken. Comparison between the adiabatic (dashed-dotted green lines) and nonadiabatic signals indicates similar trends to those observed in Fig. 2, namely the weaker attenuation rate and higher phase speed in the latter, rationalized in the discussions in Sec. III A after Eqs. (36) and (31), respectively.

Inspecting the pressure signal in Fig. 5(a) and comparing with Fig. 2(a), we observe nearly identical forms and amplitudes for $x \gtrsim 0.005$, outside the thermal layer $[\sim O(\sqrt{\text{Kn}/\omega})]$ in Fig. 5(a), and within the acoustic layer. Recalling the chosen wall heat flux amplitude, $\overline{Q}_w^{(1)} = 0.02 \times 5p^{(0)}/2$, this agrees with the result obtained in Eq. (58) for the optimal value of $\overline{Q}_w^{(1)}$ required to achieve vibroacoustic sound cancellation. Further inspection of the velocity signal in Fig. 5(b) reveals large discrepancies between the asymptotic and finite-difference solutions in the vicinity of the wall, to the extent that the former does not satisfy the impermeability condition at $x = 0$. Indeed, while a no-penetration condition is imposed on the numerical solution in Eqs. (15)–(21), the acoustic
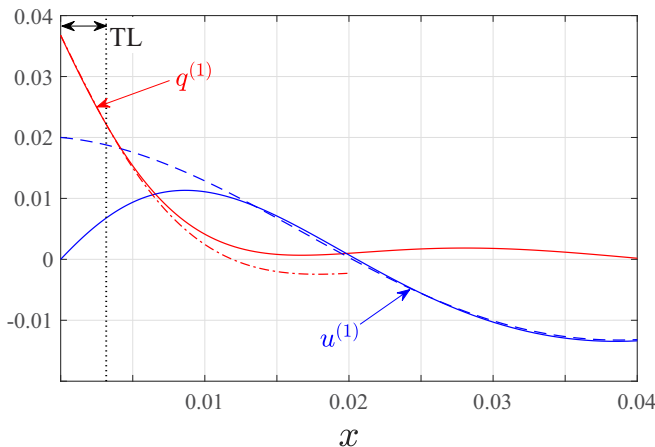
FIG. 6. Validity of the acoustic and thermal layer approximations in the case of thermoacoustic wall excitation: variations with x of the velocity (blue lines) and heat-flux (red curves) perturbations for a hard-sphere gas at $R_T = 2$ and $\text{Kn} = 10^{-3}$ subject to wall excitation with $\overline{Q}_w^{(1)} = 0.02 \times 5p^{(0)}/2$, $\overline{U}_w^{(1)} = 0$, and $\omega = 100$. The solid, dashed, and dash-dotted lines present the finite-difference-based, acoustic layer, and thermal layer solutions, respectively. The vertical dotted line confines the $x = \sqrt{\text{Kn}/\omega}$ characteristic size of the thermal layer. The results are presented at period time, $t = 2\pi/\omega$.

layer approximation satisfies only a matching condition at the edge of the thermal layer, and is not expected to capture the correct gas response within $x \ll O(\sqrt{\text{Kn}/\omega})$.

To gain further insight into the effect of the thermal-layer matching condition on the acoustic layer solution, Fig. 6 presents variations with x of the velocity (blue lines) and heat-flux (red curves) perturbations for a hard-sphere gas at $\text{Kn} = 10^{-3}$ subject to thermoacoustic wall excitation with amplitude $\overline{Q}_w^{(1)} = 0.02 \times 5p^{(0)}/2$ and frequency $\omega = 100$. The solid, dashed, and dash-dotted lines present the finite-difference, acoustic layer, and thermal layer solutions at time $t = 2\pi/\omega$, respectively, and the dotted vertical line marks the approximate size of the thermal layer, $x = \sqrt{\text{Kn}/\omega}$. In terms of the analysis in Sec. III B, the heat-flux perturbation amplitude inside the thermal layer is given by

$$\overline{q}_{\text{noniso}}^{(1)\text{TL}}(x) = -15\mu^{(0)}\overline{\tau}_{\text{noniso}}^{(1)\text{TL}}(x)/8.$$

Examining the approximate TL and numerical finite-difference solutions, it is observed that $q_{\text{noniso}}^{(1)}$ is approximated well by $q_{\text{noniso}}^{(1)\text{TL}}$ within the thermal layer. Then, comparing between the solid and dashed blue curves outside the layer, we find that $u_{\text{noniso}}^{(1)\text{AL}}$ converges to $u_{\text{noniso}}^{(1)}$ at larger distances from the wall. Indeed, the convergence of $u_{\text{noniso}}^{(1)\text{AL}}$ to $u_{\text{noniso}}^{(1)}$ is achieved at locations $x \gg \sqrt{\text{Kn}/\omega}$, after passing through an intermediate $x \sim \sqrt{\text{Kn}/\omega}$ region where neither the thermal nor acoustic layer approximations are valid. Similarly to Fig. 5(b), large deviations are observed between $u_{\text{noniso}}^{(1)\text{AL}}$ and $u_{\text{noniso}}^{(1)}$ inside the thermal layer, reillustrating that the acoustic layer solution does not satisfy the impermeability wall condition – but, instead, fits to cancel out the counterpart vibroacoustic $\overline{U}_w^{(1)} = 0.02$ signal satisfying $u^{(1)}(x = 0) = 0.02$ at the presented period time.

VI. CONCLUSION

We investigated the propagation of acoustic waves in a slightly rarefied gas at nonadiabatic conditions. Considering a planar slab configuration, constant wall heating was applied at the confining walls to maintain nonuniform temperature and density reference distributions. Acoustic excitation was then imposed via small-amplitude harmonic wall oscillations and normal

heat-flux perturbations. Focusing on continuum-limit conditions of small Knudsen numbers and high actuation frequencies (yet small compared with the mean collision frequency), the results indicated that the gas domain affected by wall excitation is confined to a thin acoustic layer in the vicinity of the excited boundary, and an approximate solution was derived based on asymptotic expansion of the acoustic fields. The application of thermoacoustic wall excitation necessitated the formation of an ever thinner thermal layer that governs the transformation of the wall's unsteady heat flux into acoustic waves. The results of the approximate analysis, supported by finite-difference-based and independent direct simulation Monte Carlo calculations, clarified the impacts of system nonadiabaticity and the gas kinetic model of interaction on sound propagation. Primarily, reference wall heating results in an extension of the acoustic layer and consequent sound-wave radiation over larger distances from the wall source. Considering the entire range of inverse power-law (repulsion point center) interactions, it was also found that wave attenuation is affected by the kinetic model of gas collisions, yielding stronger decay rates in gases with softer molecular interactions. This phenomenon could not be encountered in previous adiabatic reference-state studies of the continuum limit, where proper scaling of the acoustic perturbation problem yields identical formulation for all power-law models of interaction. Finally, our analysis was used to generalize the adiabatic-system findings for the amount of boundary heat flux required for the silencing of vibroacoustic sound at nonadiabatic reference conditions.

The present work examines the impact of system nonadiabaticity on sound-wave propagation in a planar setup at continuum-limit conditions. One possible extension of the model may therefore be the inclusion of surface curvature to study its impact on the results. Different from a planar configuration, acoustic excitation by finite curved bodies results in characteristic sound-wave attenuation that conserves the total energy radiated by the source. At continuum-limit conditions, this is coupled to the thermoviscous decay caused by viscous and heat dissipation effects, which should further alter the acoustic field compared with previous adiabatic-system analyses [40,41]. Consideration of the problem at noncontinuum-limit (intermediate regime) conditions, not studied in the present contribution, should incorporate application of higher-order hydrodynamic models or direct numerical solutions of the Boltzmann equation. Here, based on previous adiabatic-system investigations (e.g., Ref. [41]), it is expected that both acoustic and thermal layers will have a width similar to that of the Knudsen layer, which may prohibit similar asymptotic analysis of the problem.

APPENDIX: SOLUTION FOR $\overline{\tau}_{\mathrm{noniso}}^{(1)\mathrm{TL}}(x)$

Assuming a solution for Eq. (53) of the form

$$\overline{\tau}_{\mathrm{noniso}}^{(1)\mathrm{TL}}(x) = \sqrt{Ax + B}\,\Theta(x)$$

and substituting into Eq. (53), we obtain a second-order equation for $\Theta(x)$,

$$(Ax+B)^2 \frac{d^2\Theta}{dx^2} + A(Ax+B)\frac{d\Theta}{dx} - \frac{A^2}{4}\left[\frac{16i\omega p^{(0)}}{3A^2 \mathrm{Kn}}(Ax+B) + 1\right]\Theta = 0. \tag{A1}$$

Applying the change of variables

$$z = \frac{4}{A}\sqrt{\frac{\omega p^{(0)}}{3i\mathrm{Kn}}(Ax+B)}, \tag{A2}$$

we arrive at the Bessel equation,

$$z^2 \frac{d^2 \Theta}{dz^2} + z \frac{d\Theta}{dz^2} + (z^2 - 1)\Theta = 0, \tag{A3}$$

amenable to the general solution

$$\Theta(z) = c_J J_1(z) + c_Y Y_1(z), \tag{A4}$$

where $J_1(z)$ and $Y_1(z)$ are the first-order Bessel functions of the first and second kind, respectively. Assuming far-field decay of the solution, we set $c_J = 0$. Application of the wall condition

$$\overline{\tau}_{\mathrm{noniso}}^{(1)\mathrm{TL}}(x = 0) = -\frac{8}{15(T^{(0)})^{(n+1)/2}} \overline{Q}_w^{(1)} \tag{A5}$$

then fixes c_Y, and specifies the particular solution in Eq. (55).

---

[1] P. M. Morse, *Vibration and Sound* (McGraw-Hill, New York, 1948).

[2] L. Landau and E. Lifshitz, *Fluid Mechanics* (Pergamon, Reading, MA, 1959).

[3] D. W. Moore and E. A. Speigel, The generation and propagation of waves in a compressible atmosphere, Astrophys. J. **139**, 48 (1964).

[4] L. M. B. C. Campos, On three-dimensional acoustic-gravity waves in model non-isothermal atmosphere, Wave Motion **5**, 1 (1983).

[5] V. G. Kirtskhalia, Speed of sound in atmosphere of the earth, Open J. Acoust. **2**, 80 (2012).

[6] L. M. B. C. Campos, On waves in non-isothermal, compressible, ionized and viscous atmospheres, Int. Astron. Union Colloq. **66**, 355 (1983).

[7] S. Stefanov, P. Gospodinov, and C. Cercignani, Monte carlo simulation and navier-stokes finite difference calculation of unsteady-state rarefied gas flows, Phys. Fluids **10**, 289 (1998).

[8] N. G. Hadjiconstantinou, Sound wave propagation in transition-regime micro- and nanochannels, Phys. Fluids **14**, 802 (2002).

[9] D. Kalempa and F. Sharipov, Sound propagation through a rarefied gas confined between source and receptor at arbitrary knudsen number and sound frequency, Phys. Fluids **21**, 103601 (2009).

[10] T. Doi, Numerical analysis of the time-dependent energy and momentum transfers in a rarefied gas between two parallel planes based on the linearized boltzmann equation, J. Heat Transf. **133**, 022404 (2011).

[11] A. Manela, G. A. Radtke, and L. Pogorelyuk, On the damping effect of gas rarefaction on propagation of acoustic waves in a microchannel, Phys. Fluids **26**, 032001 (2014).

[12] Y. Sone, Effect of sudden change of wall temperature in rarefied gas, J. Phys. Soc. Jpn. **20**, 222 (1965).

[13] D. C. Wadsworth, D. A. Erwin, and E. P. Muntz, Transient motion of a confined rarefied gas due to wall heating or cooling, J. Fluid Mech. **248**, 219 (1993).

[14] A. Manela and N. G. Hadjiconstantinou, On the motion induced in a gas confined in a small-scale gap due to instantaneous boundary heating, J. Fluid Mech. **593**, 453 (2007).

[15] A. Manela and N. G. Hadjiconstantinou, Gas-flow animation by unsteady heating in a microchannel, Phys. Fluids **22**, 062001 (2010).

[16] A. Manela and L. Pogorelyuk, Cloaking via heating: Approach to acoustic cloaking of an actuated boundary in a rarefied gas, Phys. Fluids **26**, 062003 (2014).

[17] A. Manela and L. Pogorelyuk, Active noise control of a vibrating surface: Continuum and non-continuum investigations on vibroacoustic sound reduction by a secondary heat-flux source, J. Sound Vib. **358**, 20 (2015).

[18] S. G. Mallinson, C. Y. Kwok, and J. A. Reizes, Numerical simulation of micro-fabricated zero mass-flux jet actuators, Sens. Actuators A **105**, 229–236 (2003).

[19] A. Lee, V. Timchenko, G. H. Yeoh, and J. A. Reizes, Three-dimensional modelling of fluid flow and heat transfer in micro-channels with synthetic jet, Int. J. Heat Mass Transf. **55**, 198 (2012).

[20] J. Iannacci, M. Huhn, C. Tschoban, and H. Potter, RF-MEMS technology for future mobile and high-frequency applications: Reconfigurable 8-bit power attenuator tested up to 110 GHz, IEEE Electron Device Lett. **37**, 1646 (2016).

[21] J. Iannacci, Compact modelling-based coupled simulation of RF-MEMS networks for 5G and Internet of Things (IoT) applications, Microsyst. Technol. **25**, 329 (2019).

[22] K. Yu, T. Devkota, G. Beane, G. P. Wang, and G. V. Hartland, Brillouin oscillations from single Au nanoplate opto-acoustic transducers, ACS Nano **11**, 8064 (2017).

[23] T. Devkota, G. Beane, K. Yu, and G. V. Hartland, Attenuation of acoustic waves in ultrafast microscopy experiments, J. Appl. Phys. **125**, 163102 (2019).

[24] G. Swift, Thermoacoustic engines, J. Acoust. Soc. Am. **84**, 1145 (1988).

[25] P. Nika, Y. Baily, and F. Guermeur, Thermoacoustics and related oscillatory heat and fluid flows in micro heat exchangers, Int. J. Heat Mass Transf. **48**, 3773 (2005).

[26] J. L. Besnerais, A. Fasquelle, M. Hecquet, J. Pellé, V. Lanfranchi, and S. Harmand, Multiphysics modeling: electro-vibro-acoustics and heat transfer of PWM-fed induction machines, IEEE Trans. Indust. Electron. **57**, 1279 (2009).

[27] C. J. Lasance and R. M. Aarts, Synthetic jet cooling part I: overview of heat transfer and acoustics, in *24th Annual IEEE Semiconductor Thermal Measurement and Management Symposium* (IEEE, Piscataway, NJ, 2008), pp. 20–25.

[28] C. J. Lasance, R. M. Aarts, and O. Ouweltjes, Synthetic jet cooling part II: experimental results of an acoustic dipole cooler, in *24th Annual IEEE Semiconductor Thermal Measurement and Management Symposium* (IEEE, Piscataway, NJ, 2008), pp. 26–31.

[29] H. D. Arnold and I. B. Crandall, The thermophone as a precision source of sound, Phys. Rev. **10**, 22 (1917).

[30] H. Shinoda, T. Nakajima, K. Ueno, and N. Koshida, Thermally induced ultrasonic emission from porous silicon, Nature (London) **400**, 853 (1999).

[31] S. Julius, R. Gold, A. Kleiman, B. Leizeronok, and B. Cukurel, Modeling and experimental demonstration of heat flux driven noise cancellation on source boundary, J. Sound Vib. **434**, 442 (2018).

[32] F. A. McDonald and G. C. Wetsel, Generalized theory of the photoacoustic effect, J. Appl. Phys. **49**, 2313 (1978).

[33] E. Yariv and H. Brenner, Flow animation by unsteady temperature fields, Phys. Fluids **16**, L95 (2004).

[34] H. Hu, T. Zhu, and J. Xu, Model for thermoacoustic emission from solids, Appl. Phys. Lett. **96**, 214101 (2010).

[35] Y. Sone, *Molecular Gas Dynamics: Theory, Techniques, and Applications* (Birkhäuser, Boston, 2007).

[36] S. Stefanov, V. Roussinov, and C. Cercignani, Rayleigh-Bénard flow of a rarefied gas and its attractors. I. Convection regime, Phys. Fluids **14**, 2255 (2002).

[37] A. Manela and I. Frankel, On the Rayleigh-Bénard problem in the continuum limit: Effects of temperature differences and model of interaction, Phys. Fluids **17**, 118105 (2005).

[38] J. Strapasson and F. Sharipov, *Ab initio* simulation of heat transfer through a mixture of rarefied gases, Int. J. Heat Mass Transf. **71**, 91 (2014).

[39] F. Sharipov, *Rarefied Gas Dynamics: Fundamentals for Research and Practice* (Wiley, Weinheim, 2016).

[40] Y. Ben Ami and A. Manela, Acoustic field of a pulsating cylinder in a rarefied gas: Thermoviscous and curvature effects, Phys. Rev. Fluids **2**, 093401 (2017).

[41] Y. Ben-Ami and A. Manela, The sound of a pulsating sphere in a rarefied gas: continuum breakdown at short length and time scales, J. Fluid Mech. **871**, 668 (2019).

[42] G. Bird, *Molecular Gas Dynamics and the Direct Simulation of Gas Flows* (Clarendon, Oxford, 1994).

[43] Y. Ben-Ami and A. Manela, Nonlinear thermal effects in unsteady shear flows of a rarefied gas, Phys. Rev. E **98**, 033121 (2018).

[44] Y. Ben-Ami and A. Manela, Effect of heat-flux boundary conditions on the Rayleigh-Bénard instability in a rarefied gas, Phys. Rev. Fluids **4**, 033402 (2019).